THE JOURNAL OF PHYSICAL CHEMISTRY LETTERS
A JOURNAL OF THE AMERICAN CHEMICAL SOCIETY

pubs.acs.org/JPCL

Letter

Passivation of Hematite by a Semiconducting Overlayer Reduces Charge Recombination: An Insight from Nonadiabatic Molecular Dynamics

Hua Wang, Zhaohui Zhou,* Run Long, and Oleg V. Prezhdo*

Cite This: *J. Phys. Chem. Lett.* 2023, 14, 879–887

Read Online

ACCESS | Metrics & More | Article Recommendations | Supporting Information

ABSTRACT: Hematite (α-Fe_2O_3) is a promising photoanode material for photoelectrochemical water splitting. Surface-passivating layers are effective in improving water oxidation kinetics; however, the passivation mechanism is not fully understood due to the complexity of interfacial reactions. Focusing on the Fe-terminated Fe_2O_3 (0001) surface that exhibits surface states in the band gap, we perform ab initio quantum dynamics simulations to study the effect of an α-Ga_2O_3 overlayer on charge recombination. The overlayer eliminates surface states and suppresses charge recombination 4-fold. This explains in part the observed cathodic shift in the onset potential for water oxidation. The increased charge carrier lifetime is an outcome of two factors, energy gap and electron−vibrational coupling, with a positive contribution from the former but a negative contribution from the latter. This work presents an advance in the atomistic time-domain understanding of the influence of surface passivation on charge recombination dynamics and provides guidance for designing novel α-Fe_2O_3 photoanodes.

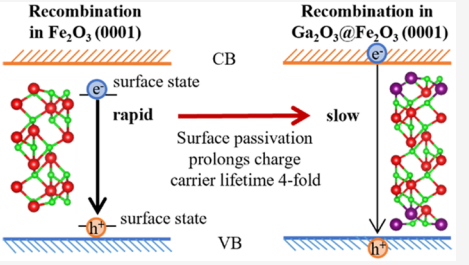

Photoelectrochemical (PEC) water splitting, which uses abundant sunlight and water as feedstock to produce hydrogen,[1] converts sunlight into energy stored in chemical fuels, providing a strategy to meet the growing energy demand and mitigate the current environmental pollution.[2,3] Among various photoanode materials, hematite (α-Fe_2O_3, hereafter Fe_2O_3) has been proved an ideal candidate for PEC water oxidation owing to its favorable properties, such as suitable band gap (~2.1 eV), high chemical stability, natural abundance, nontoxicity, and low cost.[4,5] To obtain more efficient Fe_2O_3 photoanodes, significant research has been performed over the last few decades.[6,7] However, the practical efficiencies of Fe_2O_3 photoanodes are still far below the theoretical limit.[8] Many factors have been verified, including low charge mobility,[9] slow surface reaction kinetics,[10,11] and ultrafast charge recombination.[12,13] In particular, the rapid charge recombination caused by short lifetimes of excited states severely hinders the efficiency of Fe_2O_3 photoanodes for PEC water splitting.

Fe_2O_3 exhibits ultrafast, nonradiative, and multiexponential decays in excited states[14−16] with the typical lifetime 3 orders of magnitude smaller than that in TiO_2.[17] With the emergence of PEC solar fuel conversion, the dynamics of photogenerated holes in operational Fe_2O_3 photoanodes got a lot of attention and was investigated with transient absorption spectroscopy.[18−20] Considerable progress has been made on the charge carrier dynamics in Fe_2O_3 photoanodes, such as the interrelation between the charge carrier lifetime, external electric bias, and interfacial water oxidation reaction. However, it is extremely difficult in experiments to decouple the bulk and surface effects and identify explicitly the chemical nature of surface states which is likely to have a substantial part in the interfacial reactions. Using nonadiabatic molecular dynamics (NAMD) simulations, our previous work established the charge recombination mechanisms in bulk Fe_2O_3 that contain oxygen vacancies or electron polarons, achieved the lifetimes of charge carriers which match well with the experiments, and thus bridged effectively the gap between theory and experiment.[21,22] Nevertheless, the water oxidation reaction occurs at the electrode surface, and the surface charge recombination processes should be more relevant.

It has been reported in previous publications that the surface states of Fe_2O_3 play a key role in water oxidation at Fe_2O_3 photoanodes.[23,24] In the literature, the surface states of Fe_2O_3 can be divided into two types, which have distinct effects in the water oxidation reaction.[25,26] While one type explained the surface states arising from the reaction intermediates,[27−29] the other type considered the surface states as charge recombination sites.[30−32] The former surface states depend on the reaction mechanism and are intrinsically difficult to modulate. The latter act as charge recombination sites and can be

Received: November 30, 2022
Accepted: January 16, 2023
Published: January 20, 2023

eliminated by surface modification, such as deposition of surface-passivating overlayers without catalytic activity. The surface-passivating strategy has at least three positive effects on water oxidation, namely, suppression of direct charge recombination via surface states, relief of the Fermi level pinning effect, and enhancement of charge separation due to the formation of heterostructures at the surface.[33,34] As a typical example, Formal et al. reported that an ultrathin Al_2O_3 overlayer can improve the performance of water oxidation at nanostructured Fe_2O_3 photoanodes by reducing the reaction overpotential as much as 100 mV.[31] The main cause was attributed to passivation of the surface states by the Al_2O_3 overlayer, with the enhanced radiative recombination implying that the nonradiative recombination via surface states was retarded. Neufeld et al. used density functional theory (DFT) to study the role of the Al_2O_3 overlayer on Fe_2O_3 in the water oxidation reaction and attributed the enhancement to the elevated valence band which is favorable for hole transfer.[35] Furthermore, Hisatomi et al. also reported in the experiment that deposition of ultrathin Al_2O_3, Ga_2O_3, and In_2O_3 overlayers on Fe_2O_3 photoanodes can optimize the water oxidation reaction, with the Ga_2O_3 overlayer exhibiting the most significant cathodic shift in the onset potential for PEC water oxidation.[32] The cathodic shift was also ascribed to a decrease in the density of surface states. Ulman et al. confirmed with DFT calculations that the Ga_2O_3 overlayer with a thickness of 1−2 atomic layers could eliminate the surface states[36] while making the photogenerated holes available at the active sites for water oxidation.[37]

The passivation strategy has been deemed as a critical tool for improving the performance of water oxidation at Fe_2O_3 photoanodes.[24] However, it is clear at the current stage that the static calculations can only account for part of the effects introduced by the passivating overlayer. The charge recombination dynamics has not been studied by simulations to date, due to the high complexity in the methodology and implementation, leading to a lack of direct evidence which can corroborate the role of the passivating overlayer in the surface charge recombination.

In this letter, we report simulations on the charge recombination in Fe_2O_3 (0001) surfaces with and without a Ga_2O_3 overlayer by using ab initio nonadiabatic (NA) molecular dynamics (MD). The Fe termination of Fe_2O_3 (0001) is introduced as a simple model, which has been demonstrated as the most stable phase in ambient oxygen conditions[38−40] and possibly an intermediate during water oxidation.[37,41] Our simulations indicate that deposition of an atomic overlayer of Ga_2O_3 slows down the charge recombination and prolongs the lifetime of the photogenerated charge carriers 4-fold. Among various factors, the energy gap between the valence band maximum (VBM) and the conduction band minimum (CBM) was found to be dominant for the surface charge recombination. The simulations are consistent with the transient absorption experiments[20] and rationalize in part the cathodic shift in the onset potential observed in the PEC experiments.[32]

The NAMD simulations were performed with the Python eXtension for Ab Initio Dynamics (PYXAID) software in a mixed quantum-classical framework.[42,43] The motion of nuclei is described in a semiclassical way, while the motion of electrons that are 3 orders of magnitude lighter than the nuclei is treated quantum mechanically. The original fewest switches surface hopping (FSSH)[44,45] method is difficult to implement for the NAMD simulations for multielectron condensed matter systems. The FSSH approach employing time-dependent Kohn−Sham (TDKS)[46] theory was used in this work (Sections S1 and S2, Part A of SI). Instead of the on-the-fly trajectory generation in the original FSSH, the classical path approximation (CPA)[42] was introduced into FSSH to reduce the computational cost. The CPA has been justified in the cases in which the nuclear dynamics is dominated by atomic thermal vibrations, and a single-electron excitation has a minor influence on the electron density and nuclear geometry. The velocity rescaling and hop rejection step in the original FSSH was also cast away. Instead, the detailed balance between the electronic transitions upward and downward in energy was achieved by multiplying the transition probability for upward hops by a Boltzmann factor.

The FSSH method treating nuclear motions classically excludes the loss of coherence in the electronic subsystem caused by divergence of the nuclear wave packets correlated with different electronic states. To account for the decoherence effect, the decoherence-induced surface hopping (DISH)[43] method was used (Section S3, Part A of SI). The necessity of incorporating the decoherence effect in NAMD simulations has been justified in the case that the decoherence is faster than the electronic transition[47] and verified by modeling excited-state dynamics for a wide range of systems, such as graphane,[48] black phosphorus,[49,50] TiO_2 nanotube,[51] metal halide perovskites,[52−55] etc.[56−63]

The NA coupling (NAC) is a critical factor to determine electron transitions between different potential energy surfaces in NAMD. In the FSSH-TDKS approach, a set of adiabatic KS orbitals were used to expand the TDKS orbitals. However, the phase of the adiabatic KS orbital cannot be guaranteed to be consistent along evolution of the nuclear geometry. The phase inconsistency enters the NAC and can adversely affect the NA dynamics. To eliminate this effect, a simple phase correction scheme was proposed by Akimov,[64] and the formalism therein was employed in this work (Section S4, Part A of SI).

The pseudopotential technique, for example, the projector augmented wave (PAW) method,[65,66] is a key to implementing ab initio density functional theory (DFT) for condensed matter systems. However, the adiabatic KS orbitals, namely, the pseudo wave functions, are not simple eigenstates of the one-electron KS equations and thus are nonorthogonal, giving rising to an error in the NAC computed with these orbitals. An all-electron (AE) correction scheme was developed by Chu et al. to accurately calculate the NAC by constructing the AE wave function from the pseudo wave function.[67] The AE correction is necessary in the case that the subshell d-electrons of transition metals are involved in an electron transition (Section S5, Part A of SI).

Fe_2O_3 exhibits an antiferromagnetic ground state.[68,69] The slab model was used to simulate the Fe_2O_3 (0001) surface with Fe termination and the Fe_2O_3 (0001) surface covered with the Ga_2O_3 overlayer, denoted as Fe_2O_3 (0001) and Ga_2O_3@Fe_2O_3 (0001), respectively. Five, seven, and nine atomic layers of Fe_2O_3 were used for constructing the slabs to check the effect of slab thickness on the surface properties, such as the surface stability and states. As an example, the upper panels of Figure 1 show the geometric structure of the slab with five atomic layers of Fe_2O_3 in depth and a (2 × 2) periodicity in the surface plane. For Ga_2O_3@Fe_2O_3 (0001), the slab was built by placing an atomic layer of Ga_2O_3 on both sides of the Fe_2O_3 (0001) slab (see the lower panels of Figure 1). For both surfaces, a

https://doi.org/10.1021/acs.jpclett.2c03643
J. Phys. Chem. Lett. 2023, 14, 879−887

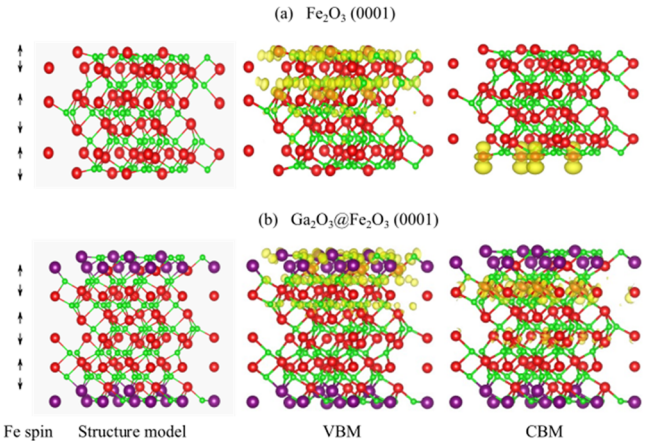

Figure 1. Optimized geometric structures, and spin-up VBM and CBM charge densities for (a) Fe_2O_3 (0001) and (b) Ga_2O_3@Fe_2O_3 (0001). The latter structure was generated by placing an atomic layer of Ga_2O_3 on both sides of the Fe_2O_3 (0001) slab. Green, red, and purple balls denote O, Fe, and Ga atoms, respectively. The charge density in yellow was visualized with the VESTA software[70] with the isosurface value set to 0.001 e/bohr^3. The partial charge density distributions for the spin-down states are symmetric to those for the spin-up states and thus not shown here.

vacuum layer of 12 Å in the normal direction was added to remove the artificial interactions between adjacent images. The size of the simulation cell in *a*, *b*, and *c* axes is 10.056, 10.056, and 22.871 Å, respectively.

The electronic structure calculations were performed with spin-polarized DFT[71,72] using the Vienna Ab initio Simulation Package (VASP) code.[73−75] The PAW[65,66] method was adopted to describe the interaction between electrons and ion cores. The generalized gradient approximation in the formalism of Perdew, Burke, and Ernzerhof (PBE)[76] was employed to deal with electron exchange and correlation. The plane wave basis set was used to expand the electron wave function with a kinetic energy cutoff of 400 eV, which has been verified to be sufficient to describe the ground state for bulk Fe_2O_3 and Ga_2O_3 (Section S6, Part A of SI). The on-site Coulomb correction[77] in the form of PBE+*U* was imposed on the Fe 3d orbitals to treat the strong electron correlation of Fe_2O_3, and the parameters *U* of 5.0 eV and *J* of 1.0 eV well reproduced the lattice constants and the band gap of bulk Fe_2O_3.[78] The Brillouin zone was sampled with a k-point grid mesh of 4 × 4 × 1 for the electronic self-consistent field calculation and 8 × 8 × 1 for accurate DOS calculation. The structural relaxation was stopped if the residual forces on each atom were less than 0.05 eV/Å.

The canonical ensemble (NVT) was employed to perform the ab initio (adiabatic) molecular dynamics (AIMD) simulations on Fe_2O_3 (0001) and Ga_2O_3@Fe_2O_3 (0001) with the target temperature of 300 K controlled by the Nose−Hoover thermostat. Only the Γ-point was used to sample the Brillouin zone. 5 ps trajectories were generated for the two systems using the Verlet algorithm with the time step of 1 fs.

The NAMD simulations were performed for 20 ps with 200 initial conditions and 1000 stochastic realizations for each condition. NACs were calculated over a period of 1 ps which was extracted from the latter half of the two trajectories. Since the latter halves of the trajectories were already in thermal equilibrium, properly representing thermal fluctuation, the NACs were replicated multiple times to meet the requirement for long NAMD simulation.

The surface energy, E_{surf}, was calculated to evaluate the surface stability of Fe_2O_3 (0001) and Ga_2O_3@Fe_2O_3 (0001) according to eq 1[36]

$$E_{surf} = \frac{1}{2A}\left(E_{slab} - \frac{1}{2}N_{Fe}E_{Fe_2O_3} - \frac{1}{2}N_{Ga}E_{Ga_2O_3}\right) \quad (1)$$

Here, E_{slab} is the energy of the slab; $E_{Fe_2O_3}$ and $E_{Ga_2O_3}$ are the energies per formula unit for bulk Fe_2O_3 and Ga_2O_3; N_{Fe} and N_{Ga} are the number of Fe and Ga atoms in the slab; and *A* is the surface area of the slab. The calculated surface energies are listed in Table 1, as functions of the slab thickness. The surface

Table 1. Surface Energy E_{surf} for Fe_2O_3 (0001) and Ga_2O_3@Fe_2O_3 (0001) with Varying Slab Thickness Defined by the Number of Atomic Layers of Fe_2O_3

	E_{surf}(meV/Å^2)			
Slab thickness	Fe_2O_3 (0001)		Ga_2O_3@Fe_2O_3 (0001)	
5	74	63[a]	76	55[a]
7	73		75	
9	72		74	

[a]Denotes reference 36.

energy changes little with the slab thickness for both Fe_2O_3 (0001) and Ga_2O_3@Fe_2O_3 (0001). The two surface energies are similar and are less than 80 meV/Å^2, indicating a good overall surface stability. Both surface energies are larger than those from the previous report,[36] by about 10 meV/Å^2 for Fe_2O_3 (0001) and 20 meV/Å^2 for Ga_2O_3@Fe_2O_3 (0001). The small discrepancies may arise from different computational codes and setups. Besides, the charge distributions and energies for the relevant states also show negligible changes with the slab thickness considered here. Taking the computational cost into consideration, the slab thickness of five layers of Fe_2O_3 was used for the following calculations.

Figures 2 and S2, Part B of SI, show the total and projected density of states (DOS) for Fe_2O_3 (0001) and Ga_2O_3@Fe_2O_3 (0001). Compared with the DOS for bulk Fe_2O_3 shown in Figure S1, Part B of SI, two surface states appear in the band gap of Fe_2O_3 (0001). One state, formed by hybridizing O 2p and Fe 3d orbitals, is located at the top of the valence band. The other state appears 0.4 eV below the conduction band and is dominated by Fe 3d orbitals. The two surface states constitute a pair of new VBMs and CBMs and give rise to a band gap of 1.23 eV for Fe_2O_3 (0001). The charge density distributions for the two surface states are spatially well separated, with the former mainly spreading over the surface and subsurface O layers on one side of the slab (middle panel of Figure 1(a)) and the latter localized exclusively over the surface Fe layer on the other side (right panel of Figure 1(a)). The spatial separation of the two surface states stems from the magnetic configuration for Fe_2O_3 (0001) which restricts the valence band around the Fe layers with one spin direction and the bonded O layers and the conduction band around the Fe layers with the opposite spin direction. A similar phenomenon has been observed in our previous work,[21] but it becomes more noticeable in the surface calculation.

As shown in Figure 2(b), the Ga_2O_3 atomic layer changes the electronic structure of Fe_2O_3 (0001) by eliminating the two surface states. This is in line with the previous theoretical

https://doi.org/10.1021/acs.jpclett.2c03643
J. Phys. Chem. Lett. 2023, 14, 879−887

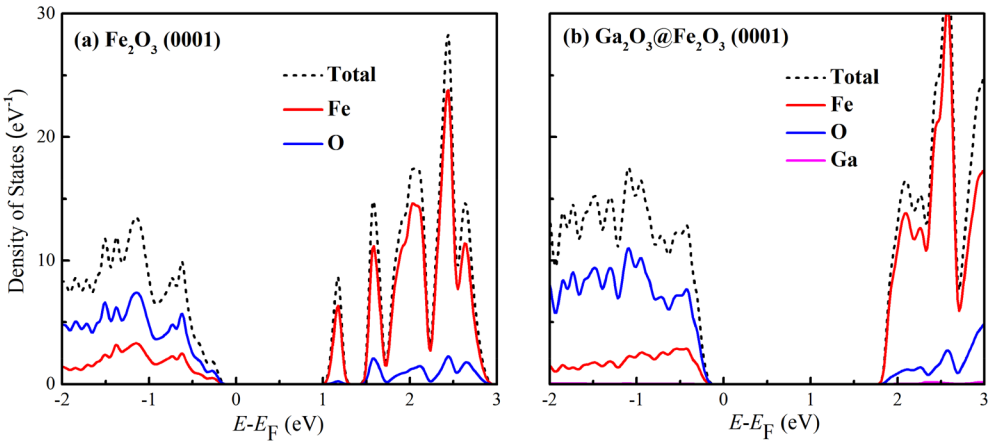

Figure 2. Density of states in the spin-up channel for (a) Fe_2O_3 (0001) and (b) Ga_2O_3@Fe_2O_3 (0001). Passivation increases the band gap by eliminating the surface states generated in the band gap of Fe_2O_3 (0001). The Fermi level is set to 0 eV.

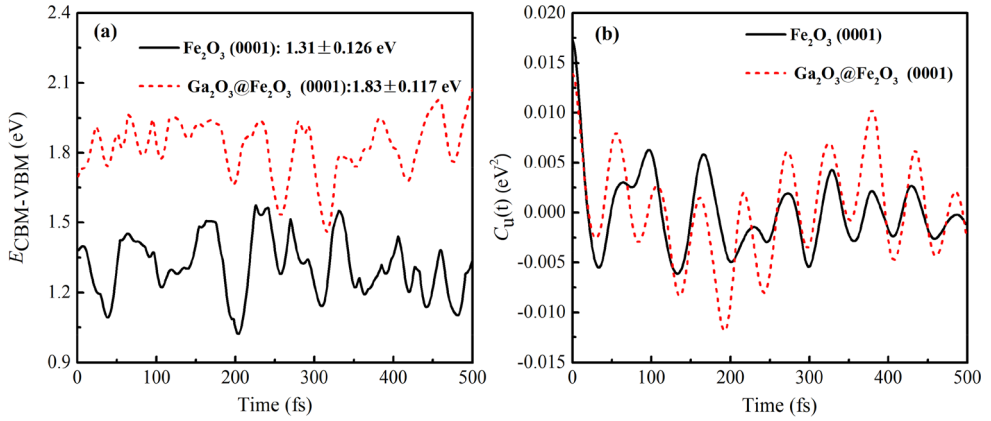

Figure 3. (a) Time evolution of the energy gaps between the VBM and CBM in the spin-up channel for Fe_2O_3 (0001) and Ga_2O_3@Fe_2O_3 (0001), with the average energies and the corresponding standard deviations shown. (b) Unnormalized ACFs of the phonon-induced fluctuations of the energy gaps.

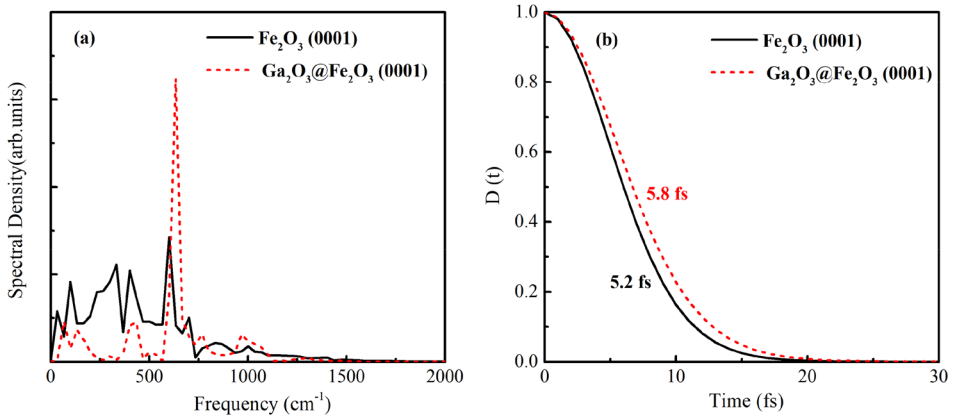

Figure 4. (a) Fourier transforms of the normalized ACFs of the phonon-induced fluctuations of the energy gaps between the VBM and CBM in the spin-up channel for Fe_2O_3 (0001) and Ga_2O_3@Fe_2O_3 (0001) and (b) pure-dephasing functions for the two surfaces.

study.[36] The constituents of the VBM and the CBM for Ga_2O_3@Fe_2O_3 (0001) are similar to those for bulk Fe_2O_3, with no contributions from Ga atoms. The Ga_2O_3 overlayer increases the band gap from 1.23 to 1.88 eV, which, however, is still less than that of bulk Fe_2O_3. The reason may be ascribed to the on-site Coulomb correction with the parameter U tested only for bulk Fe_2O_3. Surface-specific U values may be required to achieve better agreement for the band gap.[79] The charge density distributions for the VBM and the CBM also changed. The former spreads over several O layers on one side of the slab, as shown in the middle panel of Figure 1(b), while the latter is over the second Fe layer on the same side, as shown in the right panel of Figure 1(b). As a result, Ga_2O_3@Fe_2O_3 (0001) exhibits a large overlap between the VBM and the CBM compared to Fe_2O_3 (0001).

https://doi.org/10.1021/acs.jpclett.2c03643
J. Phys. Chem. Lett. 2023, 14, 879−887

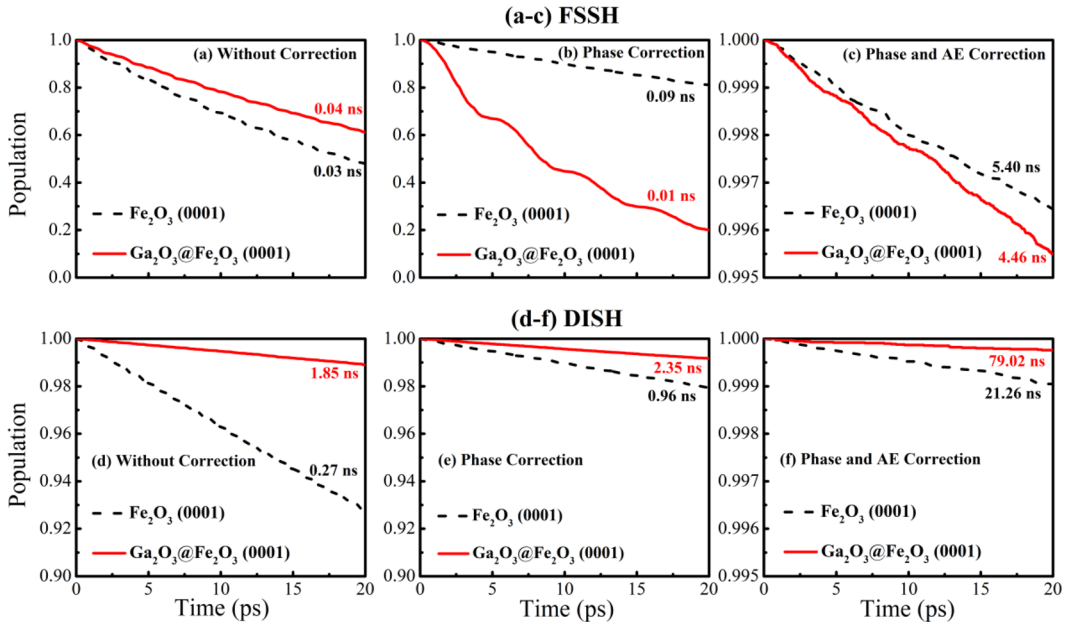

Figure 5. Population evolution of the CBM in the spin-up channel for Fe_2O_3 (0001) and Ga_2O_3@Fe_2O_3 (0001) simulated by using the FSSH and DISH methods with the NACs obtained (a, d) without correction, (b, e) with phase correction, and (c, f) with phase and AE correction. Note that the scales of the *y* axes in the panels are different.

Figures 3(a) and S3(a), Part B of SI, display time evolution of the energy gaps between the VBM and the CBM for Fe_2O_3 (0001) and Ga_2O_3@Fe_2O_3 (0001). The energy gaps fluctuate with the magnitude, close to those in bulk Fe_2O_3 containing oxygen vacancies[21] and electron polarons[22] but more strongly than that in pristine bulk Fe_2O_3.[21] The large fluctuations can be correlated with the strong electron−vibrational interaction. Compared to Fe_2O_3 (0001), Ga_2O_3@Fe_2O_3 (0001) shows a slightly weaker fluctuation of the energy gap, as demonstrated by the smaller standard deviation.

The correlation in the energy gap fluctuation can be quantified by the autocorrelation function (ACF), defined in Section S7, Part A of SI. Figures 3(b) and S3(b), Part B of SI, show the unnormalized ACFs (u-ACFs) of the phonon-induced fluctuations of the energy gaps between the VBM and the CBM for the two surfaces. Ga_2O_3@Fe_2O_3 (0001) presents a slower and more symmetric decay in the u-ACF than Fe_2O_3 (0001), likely due to elimination of the surface defect states. Long-lived coherence in the u-ACF was also observed in perfect carbon nanotubes and graphene nanoribbons.[80,81] The initial value of the u-ACF, denoting the average fluctuation of the energy gap, is smaller for Ga_2O_3@Fe_2O_3 (0001) than that of Fe_2O_3 (0001). The smaller initial value and more symmetric decay in the u-ACF contribute to a slower pure-dephasing process.[82]

The phonon influence spectrum derived from Fourier transformation of the normalized ACF gives the vibrational modes coupled to the electronic subsystem. In Figures 4(a) and S4(a), Part B of SI, Fe_2O_3 (0001) shows a broad band of vibrational modes, which is similar to those for bulk Fe_2O_3.[21] Dozens of infrared- and Raman-active vibrational modes were reported in experiments with the frequencies below 700 cm^{-1},[83] which are in coincidence with the majority of low frequency modes presented here. Ga_2O_3@Fe_2O_3 (0001) exhibits six discrete vibrational modes. The strongest mode around 630 cm^{-1} may be assigned to the longitudinal optical mode at 662 cm^{-1}[83] or the Raman-active mode at 613 cm^{-1}.[84]

The decoherence effect between a pair of electronic states is accounted for by the pure-dephasing function, $D(t)$, which is defined in Section S7, Part A of SI. The area under the u-ACF curve determines the decay of pure-dephasing functions. Figures 4(b) and S4(b), Part B of SI, show the pure-dephasing functions for Fe_2O_3 (0001) and Ga_2O_3@Fe_2O_3 (0001). They were fit well with the Gaussian function, $\exp(-t^2/2\tau_d^2)$. The fitted pure-dephasing times τ_d are quite close to each other, at 5.8 fs for Ga_2O_3@Fe_2O_3 (0001) which is slightly longer than the 5.2 fs for Fe_2O_3 (0001). In general, a short pure-dephasing time contributes to slow charge recombination due to the rapid coherence loss between the electronic state pair.[47,85]

The population evolution was simulated to characterize the charge recombination process starting from the CBM to the VBM. Figures 5 and S5, Part B of SI, show the CBM population decay for Fe_2O_3 (0001) and Ga_2O_3@Fe_2O_3 (0001) obtained using both FSSH and DISH methods, with the recombination time τ_r derived by fitting the decay curves with the first-order linear expansion to the exponential function, $\exp(-t/\tau_r)$. As expected, the DISH method renders the charge recombination process much slower in comparison to the FSSH method. Moreover, the DISH simulations offer a consistent description of the relative rate of charge recombination for the two surfaces, irrespective of corrections to NACs, as shown in Figures 5 and S5 (d, e, and f), but the FSSH simulations do not give a consistent description, as shown in Figures 5 and S5 (a, b, and c). These results make the DISH method more reliable in simulating the charge recombination processes under investigation.

The DISH simulations with the phase or AE correction to NACs give rise to slower electron−hole recombination in the two surfaces than those with no correction applied to NACs, as shown in Figures 5 and S5 (d, e, and f). The recombination time follows the order no correction < phase correction < phase and AE correction, which specifically in the spin-up channel is 0.27, 0.96, and 21.26 ns for Fe_2O_3 (0001) and 1.85, 2.35, and 79.02 ns for Ga_2O_3@Fe_2O_3 (0001), respectively. In

https://doi.org/10.1021/acs.jpclett.2c03643
J. Phys. Chem. Lett. 2023, 14, 879−887

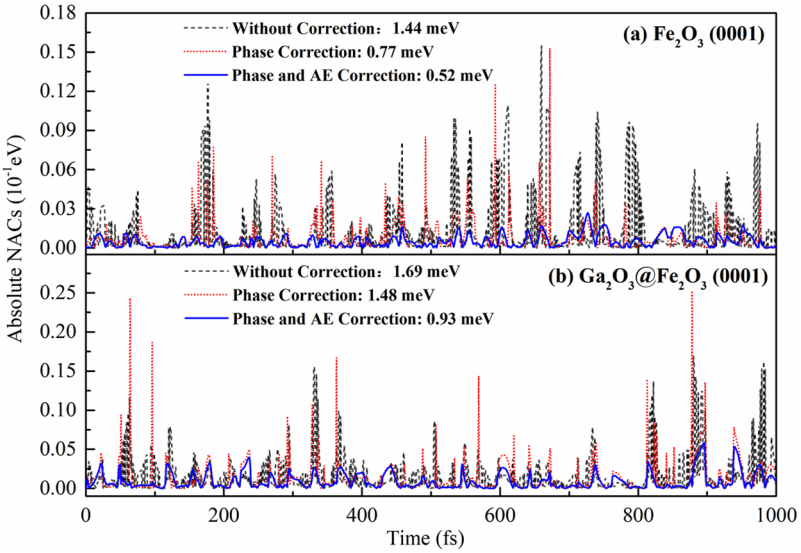

Figure 6. Effect of the phase and AE corrections on the absolute NACs in the spin-up channel for (a) Fe_2O_3 (0001) and (b) Ga_2O_3@Fe_2O_3 (0001), with the average absolute NAC values over each ensemble given to the right of the legend.

these simulations, the charge recombination rate in each surface is determined by the NAC strength. The effects of the phase and AE corrections on the NACs were inspected and shown in Figures 6 and S6, Part B of SI. Given that the NACs are complex numbers, we report here the absolute values. The uncorrected NACs show great fluctuations with many nonphysical peaks. The average values are 1.44 and 1.69 meV for Fe_2O_3 (0001) and Ga_2O_3@Fe_2O_3 (0001), respectively. The phase correction reduces the fluctuations in the NACs and gives the average values of 0.77 and 1.48 meV for the two surfaces. However, some abrupt changes in the NACs still remain. The phase correction may not be necessary to apply in this work since the two potential energy surfaces in each surface are well separated in energy.[64] The fluctuations in the NACs were further greatly suppressed by the AE correction, giving rise to smooth variations in the NACs with the average values of 0.52 and 0.93 meV. The significant improvement on the NACs demonstrates the necessity of applying the AE correction to the subshell d-electrons which are involved in the electronic transition.[67] The concentric approximation proposed by Chu and Prezhdo[86] is not considered since the NACs are already very small, although the computational efficiency can be greatly improved with the new scheme. The average absolute NAC explains well the electron−hole recombination time in each surface.

In the DISH method, three factors contribute to the charge recombination dynamics, namely, energy gap, pure dephasing time, and NAC. Generally, a larger energy gap, shorter dephasing time, and weaker NAC favor slower charge recombination, which is in line with Fermi's golden rule and the quantum Zeno effect.[47,85,87] As listed in Tables 2 and S2, Part B of SI, the Ga_2O_3 overlayer extends the surface recombination time from 21.26 to 79.02 ns in the spin-up channel and from 11.62 to 55.48 ns in the spin-down channel, prolonging the lifetime of photogenerated charge carriers by about 4 times. Transient absorption experiment indicated that while the CoO_x overlayer prolonged the photohole lifetime by 3 orders of magnitude the Ga_2O_3 overlayer only presented a modest improvement under low electric biases.[20] The observation in this experiment is thus in agreement with our

Table 2. Energy Gap, Pure-Dephasing Time, Average Absolute NAC with Phase and AE Correction, and Charge Recombination Time between the VBM and CBM in the Spin-Up Channel for Fe_2O_3 (0001) and Ga_2O_3@Fe_2O_3 (0001)

	Fe_2O_3 (0001)	Ga_2O_3@Fe_2O_3 (0001)
energy gap (eV)	1.31	1.83
pure-dephasing time (fs)	5.2	5.8
average NAC (meV)	0.52	0.93
recombination time (ns)	21.26	79.02

simulations. It can be found that the pure-dephasing times are very close to each other for the two surfaces, but Ga_2O_3@Fe_2O_3 (0001) shows a larger energy gap and stronger NAC than Fe_2O_3 (0001). The latter two factors take opposite effects on the charge recombination, which might rationalize the moderate increase in the lifetime of the photogenerated charge carriers. The larger recombination time in Ga_2O_3@Fe_2O_3 (0001) indicates that the larger energy gap plays a dominant role among the three factors in determining the surface charge recombination dynamics, despite the stronger NAC arising from a larger overlap between the VBM and the CBM in Ga_2O_3@Fe_2O_3 (0001) and reflected by the strong vibrational mode at 630 cm^{-1} (Figure 4(a)).

The PEC experiment demonstrated that deposition of an ultrathin Ga_2O_3 overlayer on Fe_2O_3 photoanodes gave birth to a cathodic shift in the onset potential for water oxidation.[32] Several factors may contribute to the cathodic shift in the onset potential, such as suppression of photogenerated charge recombination, or relief of the Fermi level pinning effect through elimination of surface states, or enhancement of charge separation due to the formation of a heterostructure at the surface.[33,34] It is a big challenge to decouple these contributions in experiments. Our simulations confirm that an atomic overlayer of Ga_2O_3 does reduce the charge recombination rate and prolongs the lifetimes of photogenerated charge carriers in Fe_2O_3 (0001), which contributes at least in part to the cathodic shift in the onset potential.

In conclusion, surface charge recombination is an important cause of energy losses in Fe_2O_3 photoanodes, severely limiting

https://doi.org/10.1021/acs.jpclett.2c03643
J. Phys. Chem. Lett. 2023, 14, 879−887

their efficiency for PEC water splitting. We considered the Fe termination of the Fe_2O_3 (0001) surface as a model system and used ab initio NAMD in combination with time-dependent Kohn−Sham theory to simulate the charge recombination dynamics in Fe_2O_3 (0001) surfaces with and without a passivating atomic overlayer of Ga_2O_3. The DISH method with the AE correction to the NACs was found to be necessary to treat this kind of electron transition which involves relatively large energy gaps and subshell d-electrons of transition metals. The simulation results show that the Ga_2O_3 overlayer slows the nonradiative charge recombination between the VBM and the CBM by ∼4 times. The reduction in the charge recombination rate contributes partly to the cathodic shift in the onset potential for water oxidation and the performance improvement for PEC water splitting with Fe_2O_3 photoanodes. Among the three factors, namely, energy gap, pure-dephasing time, and NAC strength, which contribute to the electron−hole recombination dynamics in the DISH simulations, the energy gap was found to be more important than the NAC strength, with the pure-dephasing times almost the same for the two surfaces. This work uncovers the details of charge recombination occurring at α-Fe_2O_3 surfaces and represents progress in understanding the surface charge recombination dynamics at the atomistic level and in the time domain. Such an understanding is still a big challenge to date in both experiment and simulation.

■ ASSOCIATED CONTENT

Supporting Information

The Supporting Information is available free of charge at https://pubs.acs.org/doi/10.1021/acs.jpclett.2c03643.

Part A. Supplementary Methods. S1: Time-Dependent Density Functional Theory in Kohn−Sham Formulation. S2: Fewest Switches Surface Hopping. S3: Decoherence Induced Surface Hopping. S4: Phase Correction to Nonadiabatic Coupling. S5: All-electron Correction to Nonadiabatic Coupling. S6: Verification of the Kinetic Energy Cutoff for Bulk α-Fe_2O_3 and α-Ga_2O_3. S7: Definition of Autocorrelation and Pure-Dephasing Functions. Part B. Additional Tables and Figures. Table S1: Crystal lattice constants and band gaps of bulk α-Fe_2O_3 and α-Ga_2O_3. Table S2: Energy gap, pure dephasing time, average absolute NAC, and charge recombination times in the spin-down channel. Figure S1: DOS for bulk α-Fe_2O_3 and α-Ga_2O_3. For the two surfaces in the spin-down channel. Figure S2: DOS. Figure S3: Unnormalized ACFs. Figure S4: Influence spectra and pure dephasing function. Figure S5: Results of NAMD simulations. Figure S6: Effects of phase and AE correction on the absolute NACs (PDF)

■ AUTHOR INFORMATION

Corresponding Authors

Zhaohui Zhou − *Department of Chemical Engineering, School of Water and Environment, Chang'an University, Xi'an 710064, China;* orcid.org/0000-0002-9131-6136; Email: zzhlax@chd.edu.cn

Oleg V. Prezhdo − *Deparment of Chemistry, University of Southern California, Los Angeles, California 90089, United States;* orcid.org/0000-0002-5140-7500; Email: prezhdo@usc.edu

Authors

Hua Wang − *Department of Chemical Engineering, School of Water and Environment, Chang'an University, Xi'an 710064, China*

Run Long − *College of Chemistry, Key Laboratory of Theoretical & Computational Photochemistry of Ministry of Education, Beijing Normal University, Beijing 100875, China;* orcid.org/0000-0003-3912-8899

Complete contact information is available at: https://pubs.acs.org/10.1021/acs.jpclett.2c03643

Notes

The authors declare no competing financial interest.

■ ACKNOWLEDGMENTS

Z.H.Z. acknowledges support from the Natural Science Basic Research Program of Shaanxi Province (2019JQ-440). R.L. acknowledges support from the National Natural Science Foundations of China (No. 51861135101). O.V.P. acknowledges support from the USA National Science Foundation (CHE-2154367).

■ REFERENCES

(1) Wu, N.; Lee, M. Enhanced TiO_2 Photocatalysis by Cu in Hydrogen Production from Aqueous Methanol Solution. *Int. J. Hydrogen Energy* **2004**, *29*, 1601−1605.

(2) Hisatomi, T.; Kubota, J.; Domen, K. Recent Advances in Semiconductors for Photocatalytic and Photoelectrochemical Water Splitting. *Chem. Soc. Rev.* **2014**, *43*, 7520−7535.

(3) Walter, M. G.; Warren, E. L.; McKone, J. R.; Boettcher, S. W.; Mi, Q.; Santori, E. A.; Lewis, N. S. Solar Water Splitting Cells. *Chem. Rev.* **2010**, *110*, 6446−6473.

(4) Sivula, K.; Le Formal, F.; Gratzel, M. Solar Water Splitting: Progress Using Hematite (α-Fe_2O_3) Photoelectrodes. *ChemSusChem* **2011**, *4*, 432−449.

(5) Kronawitter, C. X.; Zegkinoglou, I.; Shen, S. H.; Liao, P.; Cho, I. S.; Zandi, O.; Liu, Y. S.; Lashgari, K.; Westin, G.; Guo, J. H.; et al. Titanium Incorporation into Hematite Photoelectrodes: Theoretical Considerations and Experimental Observations. *Energy Environ. Sci.* **2014**, *7*, 3100−3121.

(6) Tilley, S. D.; Cornuz, M.; Sivula, K.; Gratzel, M. Light-Induced Water Splitting with Hematite: Improved Nanostructure and Iridium Oxide Catalysis. *Angew. Chem., Int. Ed.* **2010**, *49*, 6405−6408.

(7) Najaf, Z.; Nguyen, D. L. T.; Chae, S. Y.; Joo, O.-S.; Shah, A. U. H. A.; Vo, D.-V. N.; Nguyen, V.-H.; Le, Q. V.; Rahman, G. Recent Trends in Development of Hematite (α-Fe_2O_3) as an Efficient Photoanode for Enhancement of Photoelectrochemical Hydrogen Production by Solar Water Splitting. *Int. J. Hydrogen Energy* **2021**, *46*, 23334−23357.

(8) Murphy, A.; Barnes, P.; Randeniya, L.; Plumb, I.; Grey, I.; Horne, M.; Glasscock, J. Efficiency of Solar Water Splitting Using Semiconductor Electrodes. *Int. J. Hydrogen Energy* **2006**, *31*, 1999−2017.

(9) Rosso, K. M.; Smith, D. M. A.; Dupuis, M. An Ab Initio Model of Electron Transport in Hematite (α-Fe_2O_3) Basal Planes. *J. Chem. Phys.* **2003**, *118*, 6455−6466.

(10) Klahr, B.; Gimenez, S.; Fabregat-Santiago, F.; Bisquert, J.; Hamann, T. W. Electrochemical and Photoelectrochemical Investigation of Water Oxidation with Hematite Electrodes. *Energy Environ. Sci.* **2012**, *5*, 7626−7636.

(11) Klahr, B.; Gimenez, S.; Fabregat-Santiago, F.; Hamann, T.; Bisquert, J. Water Oxidation at Hematite Photoelectrodes: The Role of Surface States. *J. Am. Chem. Soc.* **2012**, *134*, 4294−4302.

(12) Ahmed, M. G.; Kretschmer, I. E.; Kandiel, T. A.; Ahmed, A. Y.; Rashwan, F. A.; Bahnemann, D. W. A Facile Surface Passivation of

Hematite Photoanodes with TiO_2 Overlayers for Efficient Solar Water Splitting. *ACS Appl. Mater. Interfaces* **2015**, *7*, 24053−24062.
(13) Wang, D.; Zhang, X.-T.; Sun, P.-P.; Lu, S.; Wang, L.-L.; Wei, Y.-A.; Liu, Y.-C. Enhanced Photoelectrochemical Water Splitting on Hematite Thin Film with Layer-by-Layer Deposited Ultrathin TiO_2 Underlayer. *Int. J. Hydrogen Energy* **2014**, *39*, 16212−16219.
(14) Cherepy, N. J.; Liston, D. B.; Lovejoy, J. A.; Deng, H.; Zhang, J. Z. Ultrafast Studies of Photoexcited Electron Dynamics in γ- and α-Fe_2O_3 Semiconductor Nanoparticles. *J. Phys. Chem. B* **1998**, *102*, 770−776.
(15) Joly, A. G.; Williams, J. R.; Chambers, S. A.; Xiong, G.; Hess, W. P.; Laman, D. M. Carrier Dynamics in α-Fe_2O_3 (0001) Thin Films and Single Crystals Probed by Femtosecond Transient Absorption and Reflectivity. *J. Appl. Phys.* **2006**, *99*, 053521.
(16) Sorenson, S.; Driscoll, E.; Haghighat, S.; Dawlaty, J. M. Ultrafast Carrier Dynamics in Hematite Films: The Role of Photoexcited Electrons in the Transient Optical Response. *J. Phys. Chem. C* **2014**, *118*, 23621−23626.
(17) Baxter, J. B.; Richter, C.; Schmuttenmaer, C. A. Ultrafast Carrier Dynamics in Nanostructures for Solar Fuels. *Annu. Rev. Phys. Chem.* **2014**, *65*, 423−447.
(18) Barroso, M.; Pendlebury, S. R.; Cowan, A. J.; Durrant, J. R. Charge Carrier Trapping, Recombination and Transfer in Hematite (α-Fe_2O_3) Water Splitting Photoanodes. *Chem. Sci.* **2013**, *4*, 2724−2734.
(19) Pendlebury, S. R.; Wang, X.; Le Formal, F.; Cornuz, M.; Kafizas, A.; Tilley, S. D.; Grätzel, M.; Durrant, J. R. Ultrafast Charge Carrier Recombination and Trapping in Hematite Photoanodes under Applied Bias. *J. Am. Chem. Soc.* **2014**, *136*, 9854−9857.
(20) Barroso, M.; Mesa, C. A.; Pendlebury, S. R.; Cowan, A. J.; Hisatomi, T.; Sivula, K.; Gratzel, M.; Klug, D. R.; Durrant, J. R. Dynamics of Photogenerated Holes in Surface Modified α-Fe_2O_3 Photoanodes for Solar Water Splitting. *Proc. Natl. Acad. Sci. U. S. A.* **2012**, *109*, 15640−15645.
(21) Zhou, Z.; Liu, J.; Long, R.; Li, L.; Guo, L.; Prezhdo, O. V. Control of Charge Carriers Trapping and Relaxation in Hematite by Oxygen Vacancy Charge: Ab Initio Non-Adiabatic Molecular Dynamics. *J. Am. Chem. Soc.* **2017**, *139*, 6707−6717.
(22) Cheng, C.; Zhu, Y.; Zhou, Z.; Long, R.; Fang, W.-H. Photoinduced Small Electron Polarons Generation and Recombination in Hematite. *npj Comput. Mater.* **2022**, DOI: 10.1038/s41524-022-00814-7.
(23) Liu, R.; Zheng, Z.; Spurgeon, J.; Yang, X. Enhanced Photoelectrochemical Water-Splitting Performance of Semiconductors by Surface Passivation Layers. *Energy Environ. Sci.* **2014**, *7*, 2504−2517.
(24) Zhang, J.; Eslava, S. Understanding Charge Transfer, Defects and Surface States at Hematite Photoanodes. *Sustainable Energy Fuels* **2019**, *3*, 1351−1364.
(25) Palmolahti, L.; Ali-Löytty, H.; Khan, R.; Saari, J.; Tkachenko, N. V.; Valden, M. Modification of Surface States of Hematite-Based Photoanodes by Submonolayer of TiO_2 for Enhanced Solar Water Splitting. *J. Phys. Chem.C* **2020**, *124*, 13094−13101.
(26) George, K.; Khachatrjan, T.; van Berkel, M.; Sinha, V.; Bieberle-Hütter, A. Understanding the Impact of Different Types of Surface States on Photoelectrochemical Water Oxidation: A Microkinetic Modeling Approach. *ACS Catal.* **2020**, *10*, 14649−14660.
(27) Zandi, O.; Hamann, T. W. Determination of Photoelectrochemical Water Oxidation Intermediates on Haematite Electrode Surfaces Using Operando Infrared Spectroscopy. *Nat. Chem.* **2016**, *8*, 778−783.
(28) Iandolo, B.; Hellman, A. The Role of Surface States in the Oxygen Evolution Reaction on Hematite. *Angew. Chem., Int. Ed.* **2014**, *53*, 13404−13408.
(29) Yatom, N.; Neufeld, O.; Caspary Toroker, M. Toward Settling the Debate on the Role of Fe_2O_3 Surface States for Water Splitting. *J. Phys. Chem.C* **2015**, *119*, 24789−24795.
(30) Hu, Z.; Shen, Z.; Yu, J. C. Covalent Fixation of Surface Oxygen Atoms on Hematite Photoanode for Enhanced Water Oxidation. *Chem. Mater.* **2016**, *28*, 564−572.
(31) Le Formal, F.; Tétreault, N.; Cornuz, M.; Moehl, T.; Grätzel, M.; Sivula, K. Passivating Surface States on Water Splitting Hematite Photoanodes with Alumina Overlayers. *Chem. Sci.* **2011**, *2*, 737−743.
(32) Hisatomi, T.; Le Formal, F.; Cornuz, M.; Brillet, J.; Tétreault, N.; Sivula, K.; Grätzel, M. Cathodic Shift in Onset Potential of Solar Oxygen Evolution on Hematite by 13-Group Oxide Overlayers. *Energy Environ. Sci.* **2011**, *4*, 2512−2515.
(33) Du, C.; Yang, X.; Mayer, M. T.; Hoyt, H.; Xie, J.; McMahon, G.; Bischoping, G.; Wang, D. Hematite-Based Water Splitting with Low Turn-on Voltages. *Angew. Chem., Int. Ed.* **2013**, *52*, 12692−12695.
(34) Zandi, O.; Hamann, T. W. Enhanced Water Splitting Efficiency through Selective Surface State Removal. *J. Phys. Chem. Lett.* **2014**, *5*, 1522−1526.
(35) Neufeld, O.; Yatom, N.; Caspary Toroker, M. A First-Principles Study on the Role of an Al_2O_3 Overlayer on Fe_2O_3 for Water Splitting. *ACS Catal.* **2015**, *5*, 7237−7243.
(36) Ulman, K.; Nguyen, M. T.; Seriani, N.; Gebauer, R. Passivation of Surface States of α-Fe_2O_3 (0001) Surface by Deposition of Ga_2O_3 Overlayers: A Density Functional Theory Study. *J. Chem. Phys.* **2016**, *144*, 094701.
(37) Ulman, K.; Nguyen, M.-T.; Seriani, N.; Piccinin, S.; Gebauer, R. A Unified Picture of Water Oxidation on Bare and Gallium Oxide-Covered Hematite from Density Functional Theory. *ACS Catal.* **2017**, *7*, 1793−1804.
(38) Si, Y.; Li, M.; Zhou, Z.; Liu, M.; Prezhdo, O. Improved Description of Hematite Surfaces by the SCAN Functional. *J. Chem. Phys.* **2020**, *152*, 024706.
(39) Kiejna, A.; Pabisiak, T. Surface Properties of Clean and Au or Pd Covered Hematite (α-Fe_2O_3) (0001). *J. Phys.: Condens. Matter* **2012**, *24*, 095003.
(40) Rohrbach, A.; Hafner, J.; Kresse, G. Ab Initio study of the (0001) Surfaces of Hematite and Chromia: Influence of Strong Electronic Correlations. *Phys. Rev. B* **2004**, *70*, 125426.
(41) Nguyen, M.-T.; Piccinin, S.; Seriani, N.; Gebauer, R. Photo-Oxidation of Water on Defective Hematite(0001). *ACS Catal.* **2015**, *5*, 715−721.
(42) Akimov, A. V.; Prezhdo, O. V. The Pyxaid Program for Non-Adiabatic Molecular Dynamics in Condensed Matter Systems. *J. Chem. Theory Comput.* **2013**, *9*, 4959−4972.
(43) Akimov, A. V.; Prezhdo, O. V. Advanced Capabilities of the Pyxaid Program: Integration Schemes, Decoherence Effects, Multi-excitonic States, and Field-Matter Interaction. *J. Chem. Theory Comput.* **2014**, *10*, 789−804.
(44) Tully, J. C. Molecular Dynamics with Electronic Transitions. *J. Chem. Phys.* **1990**, *93*, 1061−1071.
(45) Parandekar, P. V.; Tully, J. C. Mixed Quantum-Classical Equilibrium. *J. Chem. Phys.* **2005**, *122*, 094102.
(46) Craig, C. F.; Duncan, W. R.; Prezhdo, O. V. Trajectory Surface Hopping in the Time-Dependent Kohn-Sham Approach for Electron-Nuclear Dynamics. *Phys. Rev. Lett.* **2005**, *95*, 163001.
(47) Habenicht, B. F.; Prezhdo, O. V. Nonradiative Quenching of Fluorescence in a Semiconducting Carbon Nanotube: A Time-Domain Ab Initio Study. *Phys. Rev. Lett.* **2008**, *100*, 197402.
(48) Nelson, T. R.; Prezhdo, O. V. Extremely Long Nonradiative Relaxation of Photoexcited Graphane is Greatly Accelerated by Oxidation: Time-Domain Ab Initio Study. *J. Am. Chem. Soc.* **2013**, *135*, 3702−3710.
(49) Wei, Y.; Long, R. Grain Boundaries are Benign and Suppress Nonradiative Electron-Hole Recombination in Monolayer Black Phosphorus: A Time-Domain Ab Initio Study. *J. Phys. Chem. Lett.* **2018**, *9*, 3856−3862.
(50) Zhang, L.; Vasenko, A. S.; Zhao, J.; Prezhdo, O. V. Mono-Elemental Properties of 2D Black Phosphorus Ensure Extended Charge Carrier Lifetimes under Oxidation: Time-Domain Ab Initio Analysis. *J. Phys. Chem. Lett.* **2019**, *10*, 1083−1091.

(51) Guo, Z.; Prezhdo, O. V.; Hou, T.; Chen, X.; Lee, S. T.; Li, Y. Fast Energy Relaxation by Trap States Decreases Electron Mobility in TiO_2 Nanotubes: Time-Domain Ab Initio Analysis. *J. Phys. Chem. Lett.* **2014**, *5*, 1642−1647.
(52) Long, R.; Fang, Q.; Vasenko, A. S.; Shi, R.; Fang, W. H.; Prezhdo, O. V. Structural Disorder in Higher-Temperature Phases Increases Charge Carrier Lifetimes in Metal Halide Perovskites. *J. Am. Chem. Soc.* **2022**, *144*, 19137−19149.
(53) Shi, R.; Fang, W. H.; Vasenko, A. S.; Long, R.; Prezhdo, O. V. Efficient Passivation of DY Center in $CH_3NH_3PbBr_3$ by Chlorine: Quantum Molecular Dynamics. *Nano Research* **2022**, *15*, 2112−2122.
(54) Wu, Y. F.; Chu, W. B.; Vasenko, A. S.; Prezhdo, O. V. Common Defects Accelerate Charge Carrier Recombination in $CsSnI_3$ without Creating Mid-Gap States. *J. Phys. Chem. Lett.* **2021**, *12*, 8699−8705.
(55) Tong, C. J.; Cai, X. Y.; Zhu, A. Y.; Liu, L. M.; Prezhdo, O. V. How Hole Injection Accelerates Both Ion Migration and Nonradiative Recombination in Metal Halide Perovskites. *J. Am. Chem. Soc.* **2022**, *144*, 6604−6612.
(56) Zhu, Y. H.; Fang, W. H.; Rubio, A.; Long, R.; Prezhdo, O. V. The Twist Angle Has Weak Influence on Charge Separation and Strong Influence on Recombination in the MoS_2/WS_2 Bilayer: Ab Initio Quantum Dynamics. *J. Mater.Chem. A* **2022**, *10*, 8324−8333.
(57) Agrawal, S.; Vasenko, A. S.; Trivedi, D. J.; Prezhdo, O. V. Charge Carrier Nonadiabatic Dynamics in Non-Metal Doped Graphitic Carbon Nitride. *J. Chem. Phys.* **2022**, *156*, 094702.
(58) Zhang, P. Z.; Hou, Z. F.; Jiang, L.; Yang, J.; Saidi, W. A.; Prezhdo, O. V.; Li, W. Weak Anharmonicity Rationalizes the Temperature-Driven Acceleration of Nonradiative Dynamics in Cu_2ZnSnS_4 Photoabsorbers. *Acs Appl. Mater. Interfaces* **2021**, *13*, 61365−61373.
(59) Pal, S.; Trivedi, D. J.; Akimov, A. V.; Aradi, B.; Frauenheim, T.; Prezhdo, O. V. Nonadiabatic Molecular Dynamics for Thousand Atom Systems: A Tight-Binding Approach toward Pyxaid. *J. Chem. Theory Comput* **2016**, *12*, 1436−1448.
(60) Long, R.; Prezhdo, O. V. Asymmetry in the Electron and Hole Transfer at a Polymer-Carbon Nanotube Heterojunction. *Nano Lett.* **2014**, *14*, 3335−3341.
(61) Chaban, V. V.; Prezhdo, V. V.; Prezhdo, O. V. Covalent Linking Greatly Enhances Photoinduced Electron Transfer in Fullerene-Quantum Dot Nanocomposites: Time-Domain Ab Initio Study. *J. Phys. Chem. Lett.* **2013**, *4*, 1−6.
(62) Kamisaka, H.; Kilina, S. V.; Yamashita, K.; Prezhdo, O. V. Ab Initio Study of Temperature and Pressure Dependence of Energy and Phonon-Induced Dephasing of Electronic Excitations in CdSe and PbSe Quantum Dots. *J. Phys. Chem. C* **2008**, *112*, 7800−7808.
(63) Stier, W.; Duncan, W. R.; Prezhdo, O. V. Thermally Assisted Sub-10fs Electron Transfer in Dye-Sensitized Nanocrystalline TiO_2 Solar Cells. *Adv. Mater.* **2004**, *16*, 240−244.
(64) Akimov, A. V. A Simple Phase Correction Makes a Big Difference in Nonadiabatic Molecular Dynamics. *J. Phys. Chem. Lett.* **2018**, *9*, 6096−6102.
(65) Blöchl, P. E. Projector Augmented-Wave Method. *Phys. Rev. B* **1994**, *50*, 17953−17979.
(66) Kresse, G.; Joubert, D. From Ultrasoft Pseudopotentials to the Projector Augmented-Wave Method. *Phys. Rev. B* **1999**, *59*, 1758−1775.
(67) Chu, W.; Zheng, Q.; Akimov, A. V.; Zhao, J.; Saidi, W. A.; Prezhdo, O. V. Accurate Computation of Nonadiabatic Coupling with Projector Augmented-Wave Pseudopotentials. *J. Phys. Chem. Lett.* **2020**, *11*, 10073−10080.
(68) Punkkinen, M. P. J.; Kokko, K.; Hergert, W.; Väyrynen, I. J. Fe_2O_3 within the LSDA + U approach. *J. Phys.: Condens. Matter* **1999**, *11*, 2341−2349.
(69) Rollmann, G.; Rohrbach, A.; Entel, P.; Hafner, J. First-Principles Calculation of the Structure and Magnetic Phases of Hematite. *Phys. Rev. B* **2004**, *69*, 165107.
(70) Momma, K.; Izumi, F. Vesta 3 for Three-Dimensional Visualization of Crystal, Volumetric and Morphology Data. *J. Appl. Crystallogr.* **2011**, *44*, 1272−1276.
(71) Hohenberg, P.; Kohn, W. Inhomogeneous Electron Gas. *Phys. Rev.* **1964**, *136*, B864−B871.
(72) Kohn, W.; Sham, L. J. Self-Consistent Equations Including Exchange and Correlation Effects. *Phys. Rev.* **1965**, *140*, A1133−A1138.
(73) Kresse, G.; Hafner, J. Ab Initio Molecular Dynamics for Liquid Metals. *Phys. Rev. B Condens. Matter* **1993**, *47*, 558−561.
(74) Kresse, G.; Furthmüller, J. Efficiency of Ab-Initio Total Energy Calculations for Metals and Semiconductors Using a Plane-Wave Basis Set. *Comput. Mater. Sci.* **1996**, *6*, 15−50.
(75) Kresse, G.; Furthmuller, J. Efficient Iterative Schemes for Ab Initio Total-Energy Calculations Using a Plane-Wave Basis Set. *Phys. Rev. B Condens. Matter* **1996**, *54*, 11169−11186.
(76) Perdew, J. P.; Burke, K.; Ernzerhof, M. Generalized Gradient Approximation Made Simple. *Phys. Rev. Lett.* **1997**, *78*, 1395−1396.
(77) Liechtenstein, A. I.; Anisimov, V. V.; Zaanen, J. Density-Functional Theory and Strong Interactions: Orbital Ordering in Mott-Hubbard Insulators. *Phys. Rev. B Condens. Matter* **1995**, *52*, R5467−R5470.
(78) Zhou, Z.; Huo, P.; Guo, L.; Prezhdo, O. V. Understanding Hematite Doping with Group IV Elements: A DFT+U Study. *J. Phys. Chem. C* **2015**, *119*, 26303−26310.
(79) Huang, X.; Ramadugu, S. K.; Mason, S. E. Surface-Specific DFT +U Approach Applied to α-Fe_2O_3 (0001). *J. Phys. Chem. C* **2016**, *120*, 4919−4930.
(80) Habenicht, B. F.; Kamisaka, H.; Yamashita, K.; Prezhdo, O. V. Ab Initio Study of Vibrational Dephasing of Electronic Excitations in Semiconducting Carbon Nanotubes. *Nano Lett.* **2007**, *7*, 3260−3265.
(81) Habenicht, B. F.; Kalugin, O. N.; Prezhdo, O. V. Ab Initio Study of Phonon-Induced Dephasing of Electronic Excitations in Narrow Graphene Nanoribbons. *Nano Lett.* **2008**, *8*, 2510−2516.
(82) Liu, J.; Kilina, S.; Tretiak, S.; Prezhdo, O. V. Ligands Slow Down Pure-Dephasing in Semiconductor Quantum Dots. *ACS Nano* **2015**, *9*, 9106−9116.
(83) Onari, S.; Arai, T.; Kudo, K. Infrared Lattice Vibrations and Dielectric Dispersion in α-Fe_2O_3. *Phys. Rev. B* **1977**, *16*, 1717−1721.
(84) Chamritski, I.; Burns, G. Infrared- and Raman-Active Phonons of Magnetite, Maghemite, and Hematite: A Computer Simulation and Spectroscopic Study. *J. Phys. Chem. B* **2005**, *109*, 4965−4968.
(85) Kilina, S. V.; Neukirch, A. J.; Habenicht, B. F.; Kilin, D. S.; Prezhdo, O. V. Quantum Zeno Effect Rationalizes the Phonon Bottleneck in Semiconductor Quantum Dots. *Phys. Rev. Lett.* **2013**, DOI: 10.1103/PhysRevLett.110.180404.
(86) Chu, W.; Prezhdo, O. V. Concentric Approximation for Fast and Accurate Numerical Evaluation of Nonadiabatic Coupling with Projector Augmented-Wave Pseudopotentials. *J. Phys. Chem. Lett.* **2021**, *12*, 3082−3089.
(87) Liu, J.; Neukirch, A. J.; Prezhdo, O. V. Non-Radiative Electron−Hole Recombination in Silicon Clusters: Ab Initio Non-Adiabatic Molecular Dynamics. *J. Phys. Chem. C* **2014**, *118*, 20702−20709.

https://doi.org/10.1021/acs.jpclett.2c03643
J. Phys. Chem. Lett. 2023, 14, 879−887